medRxiv preprint doi: https://doi.org/10.1101/2024.08.12.24311885; this version posted August 13, 2024. The copyright holder for this preprint (which was not certified by peer review) is the author/funder, who has granted medRxiv a license to display the preprint in perpetuity. All rights reserved. No reuse allowed without permission.

An atlas of genetic effects on the monocyte methylome across European and African populations

Running title: Multi-ancestry monocyte methylome study

Wanheng Zhang[1,2,#], Xiao Zhang[3,#], Chuan Qiu[3], Zichen Zhang[1], Kuan-Jui Su[3], Zhe Luo[3], Minghui Liu[4], Bingxin Zhao[5], Lang Wu[6], Qing Tian[3], Hui Shen[3,*], Chong Wu[1,7,*] and Hong-Wen Deng[3,*]

[1]Department of Biostatistics, The University of Texas MD Anderson Cancer Center, Houston, TX 77030, USA.

[2]Department of Biostatistics and Data Science, School of Public Health, The University of Texas Health Science Center at Houston, Houston, TX 77030, USA

[3]Division of Biomedical Informatics and Genomics, Tulane Center of Biomedical Informatics and Genomics, Deming Department of Medicine, Tulane University, New Orleans, LA 70112, USA

[4]Department of Molecular and Cellular Oncology, The University of Texas MD Anderson Cancer Center, Houston, TX 77030, USA

[5]Department of Statistics and Data Science, University of Pennsylvania, Philadelphia, PA 19104, USA

[6]Cancer Epidemiology Division, Population Sciences in the Pacific Program, University of Hawaii Cancer Center, University of Hawaii at Manoa, Honolulu, HI, 96813, USA

[7]Institute for Data Science in Oncology, The UT MD Anderson Cancer Center, Houston, TX, 77030, USA.

[#]*These authors contribute equally*

**Corresponding authors:*

Hui Shen (hshen3@tulane.edu), Chong Wu (cwu18@mdanderson.org) and Hong-Wen Deng (hdeng2@tulane.edu)

Hui Shen, Ph.D.
Professor
Associate Director, Center for Biomedical Informatics & Genomics
Associate Director, Tulane Integrated Institute of Data and Health Sciences (TIIDHS)
School of Medicine, Tulane University
1440 Canal Street, Suite 1621, New Orleans, LA 70112, USA
Phone: 504-988-6987
Email: hshen3@tulane.edu

Chong Wu, Ph.D.
Assistant Professor
Department of Biostatistics, University of Texas MD Anderson Cancer Center
7007 Bertner Avenue, Unit 1689, Houston, TX 77030
Phone: 713-409-5160
Email: cwu18@mdanderson.org

NOTE: This preprint reports new research that has not been certified by peer review and should not be used to guide clinical practice.

medRxiv preprint doi: https://doi.org/10.1101/2024.08.12.24311885; this version posted August 13, 2024. The copyright holder for this preprint (which was not certified by peer review) is the author/funder, who has granted medRxiv a license to display the preprint in perpetuity.
All rights reserved. No reuse allowed without permission.

Hong-Wen Deng, Ph.D.
Professor
Aron Family Endowed Chair
Director, Center for Biomedical Informatics & Genomics
Director, Tulane Integrated Institute of Data and Health Sciences (TIIDHS)
School of Medicine, Tulane University
1440 Canal Street, Suite 1621, New Orleans, LA 70112, USA
Phone: 504-988-1310
Email: hdeng2@tulane.edu

medRxiv preprint doi: https://doi.org/10.1101/2024.08.12.24311885; this version posted August 13, 2024. The copyright holder for this preprint (which was not certified by peer review) is the author/funder, who has granted medRxiv a license to display the preprint in perpetuity. All rights reserved. No reuse allowed without permission.

Abstract

Elucidating the genetic architecture of DNA methylation (DNAm) is crucial for decoding the etiology of complex diseases. However, current epigenomic studies often suffer from incomplete coverage of methylation sites and the use of tissues containing heterogeneous cell populations. To address these challenges, we present a comprehensive human methylome atlas based on deep whole-genome bisulfite sequencing (WGBS) and whole-genome sequencing (WGS) of purified monocytes from 298 European Americans (EA) and 160 African Americans (AA) in the Louisiana Osteoporosis Study. Our atlas enables the analysis of over 25 million DNAm sites. We identified 1,383,250 and 1,721,167 methylation quantitative trait loci (meQTLs) in *cis*-regions for EA and AA populations, respectively, with 880,108 sites shared between ancestries. While *cis*-meQTLs exhibited population-specific patterns, primarily due to differences in minor allele frequencies, shared *cis*-meQTLs showed high concordance across ancestries. Notably, *cis*-heritability estimates revealed significantly higher mean values in the AA population (0.09) compared to the EA population (0.04). Furthermore, we developed population-specific DNAm imputation models using Elastic Net, enabling methylome-wide association studies (MWAS) for 1,976,046 and 2,657,581 methylation sites in EA and AA, respectively. The performance of our MWAS models was validated through a systematic multi-ancestry analysis of 41 complex traits from the Million Veteran Program. Our findings bridge the gap between genomics and the monocyte methylome, uncovering novel methylation-phenotype associations and their transferability across diverse ancestries. The identified meQTLs, MWAS models, and data resources are freely available at www.gcbhub.org and https://osf.io/gct57/.

medRxiv preprint doi: https://doi.org/10.1101/2024.08.12.24311885; this version posted August 13, 2024. The copyright holder for this preprint (which was not certified by peer review) is the author/funder, who has granted medRxiv a license to display the preprint in perpetuity. All rights reserved. No reuse allowed without permission.

Introduction

Unraveling the functional consequences of genetic variation on complex human diseases is a fundamental challenge in human genetics. While genome-wide association studies (GWAS) have identified more than 24,000 unique single nucleotide polymorphism (SNP)-trait associations across a range of complex diseases and traits,[1] the molecular pathways through which these variations contribute to disease risk remain largely elusive[2,3]. This knowledge gap hinders the advancement of therapeutic targets[4] and underscores the need for studying multi-omics biomarkers[5]. DNA methylation (DNAm), a relatively stable epigenetic mark, has emerged as a critical molecular biomarker in this endeavor. DNAm not only provides insights into the current state of human health[6] but also facilitates the estimation of epigenetic age[7–9] and partially captures the effects of lifestyle and environment exposures[10] on disease pathogenesis. Recognizing its potential, extensive efforts have been made to collect comprehensive, population-scale datasets of the human genome and methylome.[11–19]

However, these pursuits have been constrained by several key limitations. Firstly, the reliance on Illumina BeadChip platforms[20] restricts the analysis to only 3% of the approximately 30 million CpG sites in the human methylome[21–24], due to its focus on only 450,000 or 935,000 predefined CpG methylation sites. This constraint significantly limits our understanding of the methylome's extensive landscape. Secondly, the majority of methylation studies have examined whole blood samples[25–28] or normal bulk tissue[29–31], adjusting the estimated cell type proportions as covariates[32,33]. This approach inherently limits the examination of methylation patterns in specific cell types, which could be crucial for understanding disease mechanisms.[34,35] Monocytes, in particular, play central roles in various physiological and pathological processes, including bone remodeling[36,37], neurodegenerative disorders such as Alzheimer's disease[38,39], inflammatory conditions like rheumatoid arthritis[40] and inflammatory bowel disease, cardiovascular diseases[41], cancer[42], and infectious diseases, making them a highly relevant cell type for investigating the link between genetic variation, DNAm, and complex diseases. Thirdly, DNAm and genetic variations could be ancestry-specific[43–45], highlighting the critical need to study DNAm across multi-ancestry populations to fully characterize their relationships.

To overcome these limitations and accurately characterize the human methylome in purified monocytes across European Americans (EA) and African Americans (AA) ancestry, we performed whole genome bisulfite sequencing (WGBS) and whole genome sequencing (WGS) on 298 independent individuals of EA and 160 independent individuals of AA in the Louisiana Osteoporosis Study[46]. Our comprehensive approach encompassed several key analyses. For each ancestry group, we conducted methylation quantitative trait loci (meQTL) analyses to identify loci in both *cis*- and *trans*-region where genetic variations are associated with DNAm changes, and compared results across ancestries to explore shared and unique genetic architecture. Further, we calculated *cis*-heritability (*cis*-h^2) of DNAm to quantify the proportion of variance in methylation levels that can be explained by *cis*-acting genetic variants. To link our findings to complex traits, we conducted methylome-wide association studies (MWASs) using an instrumental variable regression framework with two steps.[47,48] First, we built DNAm prediction, or imputation models using penalized regression. Second, we tested the association between the predicted DNAm and 41 phenotypes using GWAS summary statistics from the Million Veteran

medRxiv preprint doi: https://doi.org/10.1101/2024.08.12.24311885; this version posted August 13, 2024. The copyright holder for this preprint (which was not certified by peer review) is the author/funder, who has granted medRxiv a license to display the preprint in perpetuity. All rights reserved. No reuse allowed without permission.

Program (MVP) dataset[49] in both AA and EA. The results were further validated by colocalization and Mendelian randomization (MR) analyses. This multi-faceted approach provides new insights into the genetic regulation of monocyte-specific DNAm and its relationship to complex traits across diverse ancestries. The overview of our study design is presented in Fig.1, and the developed models and data resources are freely accessible at www.gcbhub.org.

Results

Data collection and processing

We recruited 495 male subjects aged 20-51 years (185 AA and 310 EA) from the ongoing Tulane Louisiana Osteoporosis Study cohort[46] with strict inclusion/exclusion criteria; see Method section and Supplementary Table 1 for details. We restricted our analyses to subjects with purified peripheral blood monocytes (PBMs). Sequencing reads were processed to remove adaptor sequences, contamination, and low-quality bases, then aligned to the human reference genome GRCh38/hg38. In total, methylation levels for over 25 million CpG sites across the genome were quantified (see Methods for details). DNAm β-values underwent rank-based inverse normal transformation[50] to normalize the data distribution. We also implemented comprehensive quality control (QC) for the genetic data. Single nucleotide polymorphisms (SNPs) were excluded based on several criteria: deviation from Hardy-Weinberg equilibrium ($P < 1 \times 10^{-6}$), minor allele frequency (MAF) less than 0.01, and presence of mismatched alleles. Additionally, to mitigate confounding effects from population structure, we removed individuals with a degree of relatedness, defined as an identity by state (IBS) greater than 0.125. This resulted in a final cohort of 160 AA and 298 EA. For the genetic data, we extracted the top ten principal components (PCs) to capture the major axes of genetic variation. Similarly, principal component analysis (PCA) was conducted on the DNAm data, focusing on the 20,000 most variable CpG sites to obtain the top ten nongenetic PCs.[11] Adjusting for nongenetic PCs derived from the DNAm data can significantly improve the power to detect true associations[51], and the risk of introducing collider bias that could impact the results is minimal[11]. As a result, a total of 13,238,663 SNPs were utilized in the AA cohort and 8,513,381 SNPs in the EA cohort.

Identification of *cis*-meQTL for whole genome DNAm sites across two populations

We conducted *cis*-meQTL analyses for independent individuals of AA (n=160) and EA (n=298) ancestries separately for the 25,721,231 CpG sites measured by WGBS. *Cis*-regions were defined as regions extending ±1 Mb from the CpG sites. Using MatrixEQTL[52], we identified *cis*-region methylation quantitative trait loci (*cis*-meQTL) by testing the association between DNAm and genotype via linear regression, adjusting for confounders including age, BMI, smoking, and alcohol consumption. Although WGBS was performed on purified PBMs with monocytes purity exceeding 90% with the average proportion of monocytes was 98.8%, the proportion can vary across samples, ranging from 90.1% to 99.9%. To account for potential source of heterogeneity from monocytes and to control for any residual contamination from other cell types, we included the estimated proportions of the three cell types with the most variation (B cells, monocytes, and neutrophils) as covariates in our analysis. Furthermore, we controlled for ten genetic and ten nongenetic principal components.

medRxiv preprint doi: https://doi.org/10.1101/2024.08.12.24311885; this version posted August 13, 2024. The copyright holder for this preprint (which was not certified by peer review) is the author/funder, who has granted medRxiv a license to display the preprint in perpetuity. All rights reserved. No reuse allowed without permission.

We identified 58,472,084 and 127,178,161 *cis*-meQTL associations ($P < 1 \times 10^{-8}$)[11] in the AA and EA populations, respectively. On average, each CpG site had 2.27 *cis*-meQTL mappings in the AA population and 4.94 in the EA population. In total, 1,721,167 CpG sites in the AA and 1,383,250 in the EA population exhibited at least one *cis*-meQTL, representing 6.7% and 5.4% of all sites tested, respectively, with 880,108 (51.1% of AA and 63.6% of EA) overlapping CpG sites across the two populations.

The analysis of *cis*-meQTL associations across two populations revealed a negative correlation between MAF and effect size (Fig. 2a). This pattern aligns with expectations based on studies in GWAS, where rarer genetic variants often exhibit larger effect sizes in quantitative trait loci studies in GWAS, despite their lower detection power due to reduced allele frequencies.[53] We further found the AA population exhibited a stronger negative correlation (coefficient $= -2.7$) compared to the EA population (coefficient $= -2.0$), along with higher median effect sizes (AA: median = 0.90, EA: median = 0.65, $P < 1 \times 10^{-16}$ by Wilcoxon sum rank test). These findings extend the general principles observed in QTL studies[53,54] to meQTL analyses and highlight notable differences between populations. Additionally, it shows a concentration of the associations with higher effect sizes clustered around the CpG sites for both AA and EA (Fig. 2b). There was also a strong negative correlation (AA: coefficient $= -1.2 \times 10^{-5}$, $P < 2 \times 10^{-16}$; EA: coefficient $= -1.1 \times 10^{-5}$, $P < 2 \times 10^{-16}$) between p-values of *cis*-meQTL associations and the distance from the CpG site for both ancestries (Supplementary Fig. 1).

We also investigated the distribution of *cis*-meQTLs associated with each CpG site residing in different annotated genomic regions using Annotatr[55] Bioconductor package for AA and EA populations separately. Among all the CpG sites having at least one *cis*-meQTL, 0.9% (AA) and 1.1% (EA) were located in CpG islands and 4.4% (AA) and 4.8% (EA) in CpG-adjacent regions (shores and shelves), and the rest (94.7% for AA and 94.1% for EA) were away from CpG islands (open seas) (Fig. 2c). Among all the CpG sites located in islands, 2.9% (AA) and 1.8% (EA) had at least one *cis*-meQTL. For those located in shores and shelves, 5.0% (AA) and 4.2% (EA) had at least one *cis*-meQTL. For those located in open seas, 6.9% (AA) and 5.6% (EA) had at least one *cis*-meQTL association. These findings align with current understanding that CpG sites with meQTLs are enriched in open sea regions.[18]

Interestingly, 8% of the *cis*-meQTLs in the EA population were either nonexistent or rare, defined as two or fewer individuals carrying the variant, in the Phase-3 1000 Genome Project[56] (1000G) African population, while 30% in the AA population were rare or nonexistent in the 1000G European population. For the sentinel *cis*-meQTLs, defined as the most significant SNP for each CpG, 19% in the EA were rare or nonexistent in the 1000G African population, while 49% in the AA were rare or nonexistent in the 1000G European population (Fig. 2d). This underscores the importance of leveraging data from diverse and specific ancestries to uncover ancestry-specific *cis*-meQTLs, highlighting distinct genetic variations and their specific implications in DNAm across populations. For *cis*-meQTLs identified in both ancestries, the effect sizes exhibited a high degree of concordance (correlation$= 0.96, P < 2 \times 10^{-16}$, Fig. 2e).

medRxiv preprint doi: https://doi.org/10.1101/2024.08.12.24311885; this version posted August 13, 2024. The copyright holder for this preprint (which was not certified by peer review) is the author/funder, who has granted medRxiv a license to display the preprint in perpetuity. All rights reserved. No reuse allowed without permission.

To identify the causal variants underlying significant *cis*-meQTL for methylation, we conducted population-specific fine-mapping for 1,655,943 and 1,334,508 CpG sites with at least one *cis*-meQTL in AA and EA populations using SuSiE[57]. We found that the number of variants within the 95% credible sets was notably smaller for the AA population, with a median of 13 and an interquartile range (IQR) of 8,045, as opposed to the EA population, which exhibited a median of 27 and an IQR of 5,316 (Fig. 2f). This result is consistent with findings from a previous pQTL study[54] for plasma proteins and may be attributed to the lower average linkage disequilibrium (LD) in the AA population or the smaller sample size of the AA cohort compared to the EA cohort.

Cis-h^2 of CpG sites and imputation models

We estimated *cis*-h^2, i.e., the proportion of methylation variance attributable to genetic factors of DNAm, using restricted maximum likelihood (REML) in GCTA[58]. Among all the 25,721,231 CpG sites in WGBS, we found that 50.5% and 57.0% CpG sites exhibited a *cis*-h^2 greater than 0.01, 21.1% and 33.8% CpG sites with a *cis*-h^2 between 0.01 and 0.1, and 28.3% and 9.2% CpG sites with a *cis*-h^2 greater than 0.1 for the AA and EA populations, respectively (Fig. 3a). The mean values for *cis*-h^2 of AA population (0.09) is significantly higher than that of EA population (0.04) ($P < 1 \times 10^{-16}$ by a Wilcoxon sum rank test). Besides, we investigated the p-values for the *cis*-h^2 estimated from REML and found that among CpG sites with *cis*-h^2 greater than 0.01, 16.4% and 18.2% of them having p-values less than 0.05, while among CpG sites with *cis*-h^2 greater than 0.5, 36.8% and 55.1% of them having p-values less than 0.05, for AA and EA respectively (Fig. 3b).

For CpG sites with a *cis*-h^2 greater than 0.1, 20% in the AA population and 42% in the EA population were also identified with *cis*-meQTLs in our study. Furthermore, the majority of CpG sites with a *cis*-h^2 exceeding 0.5 showed *cis*-meQTL associations (86% for AA and 99% for EA) as illustrated in Fig. 3c. The mean value of *cis*-h^2 in CpG sites with at least one *cis*-meQTLs (0.48 for AA and 0.33 for EA) was also larger than those without *cis*-meQTLs (0.06 for AA and 0.02 for EA) (Fig. 3d). This is expected as CpG sites with higher *cis*-h^2 are more likely to be associated with *cis*-SNPs.

Notably, a seeming contradiction arises: the *cis*-h^2 in the AA ancestry is higher than that in the EA ancestry, yet fewer *cis*-meQTL associations are identified in the AA ancestry compared to the EA ancestry. We hypothesize that this discrepancy is attributed to the smaller sample size in the AA population. To test this hypothesis, we randomly sampled 160 individuals from the EA population and conducted *cis*-meQTL analysis. This analysis resulted in 48,086,725 associations, averaging 1.87 *cis*-meQTL associations per CpG site in the EA population, which is lower than the 2.27 *cis*-meQTL associations per site observed in the AA population. This finding indicates that the apparent contradiction is indeed a consequence of the differing sample sizes between the populations, highlighting the importance of collecting more data in AA.

Furthermore, *cis*-h^2 assessments were performed on WGBS DNAm, focusing on CpG sites covered by two platforms: the MethylationEPIC Infinium v2.0[59], which contains over 935,000 CpG sites (referred to as the 900K set), and the HumanMethylation450 Infinium assay[60], encompassing around 450,000 sites (referred to as the 450K set). Recent update from EPIC to

medRxiv preprint doi: https://doi.org/10.1101/2024.08.12.24311885; this version posted August 13, 2024. The copyright holder for this preprint (which was not certified by peer review) is the author/funder, who has granted medRxiv a license to display the preprint in perpetuity. All rights reserved. No reuse allowed without permission.

EPIC v2 have complicated integrating new data with previous Infinium array platforms, such as the EPIC and the HM450K, and has been used in recent studies.[61–63] The two datasets are provided at https://zwdzwd.github.io/InfiniumAnnotation. The mean values of *cis*-h^2 of CpG sites from the 900K dataset for AA and EA ancestries were 0.08 and 0.03, respectively. Similarly, the 450K dataset showed mean values of 0.08 for AA and 0.03 for EA ancestries. The distribution of *cis*-h^2 values for CpG sites in the 450K and 900K sets closely mirrored that of the overall WGBS dataset, albeit with slightly lower values (Fig. 3e). This similarity indicates that these array-based platforms capture a representative, rather than a unique, subset of CpGs in terms of heritability patterns. Consequently, the primary advantage of WGBS lies in its broader coverage, which not only encompasses the sites captured by array-based platforms but also extends our understanding of methylation patterns across the entire genome.

Next, to conduct MWAS for complex traits, we built imputation models for CpG sites with *cis*-h^2 > 0.01 using Elastic Net[64] with nested cross-validation[65] to obtain evaluation matrices. We selected SNPs within 500 kb of CpG sites for computational efficiency. We built DNAm prediction models (with R^2 value of at least 0.01) for 2,657,581 and 1,976,046 CpG sites in AA and EA populations, with 1,067,816 overlapped CpG sites. The mean accuracy for models for DNAm prediction, measured by R^2, was 0.19 and 0.17 for AA and EA populations, respectively. Notably, the median model accuracy for CpG sites covered by the 450K and 900K arrays was 0.11 and 0.10 in AA, and 0.10 and 0.09 in EA. These R^2 values are lower than those obtained from WGBS, consistent with our heritability findings.

Multi-ancestry MWAS of complex traits in MVP

We performed a systematic multi-ancestry (EA and AA) MWAS on 41 distinct phenotypes by using GWAS summary statistics from the Million Veteran Program (MVP) dataset[49]. Similar to transcriptome-wide association studies (TWASs)[66–68] which assesses gene expression levels and their associations with traits, and proteome-wide association studies (PWASs)[3,54] that focus on the proteomic landscape to understand protein variations and their disease linkages, MWASs focus on the association between DNAm and complex traits, and operates through a two-step instrumental variable regression framework[47,48]. Utilizing a stringent significance threshold, adjusted by the Bonferroni correction across all models and phenotypes (P cutoff is 4.9×10^{-10} for AA and 6.6×10^{-10} for EA), we identified 34,334 significant methylation-phenotype associations (Supplementary Tables 2.1 and 2.2). Since the sample size of EA GWAS data (mean = 261,202) is much larger than that of AA (mean = 54,271), the results of EA accounted for majority of these associations, 31,336 to be precise, while the AA contributed 2,998 (Fig. 4a). Notably, our findings revealed that, for AA, 2,944 (98.1%) and 2,926 (97.6%) significant associations were not captured by the 450K and 900K methylation panels, respectively. Similarly, for EA, 30,835 (98.4%) and 30,394 (97.0%) associations were beyond the coverage of these panels. This highlights our study's extensive coverage, significantly encompassing a broader scope of the methylome, indicating a comprehensive mapping of methylation associations across ancestries.

Among the identified associations, 559 unique methylation-phenotype association pairs were significant in both ancestries; the majority (537 out of 559) of these associations displayed consistent directions of effects (Fig. 4b). This consistency underscores a possible shared

medRxiv preprint doi: https://doi.org/10.1101/2024.08.12.24311885; this version posted August 13, 2024. The copyright holder for this preprint (which was not certified by peer review) is the author/funder, who has granted medRxiv a license to display the preprint in perpetuity. All rights reserved. No reuse allowed without permission.

epigenetic mechanism across ancestries. These consistent associations encompassed 433 distinct DNAm sites and were observed across 12 phenotypes categorized into six broad groups: lipids, cardiovascular diseases (CVD), anthropometric measurements, metabolic conditions, renal traits, and addiction.

Further delving into the gene annotation for these consistent associations, we found a distribution of the CpG sites: 529 of the 599 consistent pairs had CpG sites in the open sea regions of the genome, indicative of potential regulatory elements in less explored genomic territories. Additionally, 30 associations had CpG sites in genomic shores, 24 in shelves, and 15 in islands. This distribution hints at the varied genomic landscapes in which significant methylation changes occur and their potential implications in diverse physiological traits and conditions.

We also mapped CpG sites from all associations to the genes and used Aggregated Cauchy Association Test (ACAT)[69] to detect significant gene-phenotype associations.[70] At a significant threshold with Bonferroni correction (P cutoff is 2.7×10^{-6} for AA and EA), we identified 8,670 significant associations for EA population encompassing 30 traits and 7 categories (Supplementary Table 3.2). We also identified 1,109 significant associations for AA population encompassing 17 traits and 7 categories (Supplementary Table 3.1). Among these, 747 associations are significant in both ancestries, and they encompassed 14 traits in 6 categories (Supplementary Table 4). By leveraging WGBS data from purified monocytes samples, our MWAS offers unique opportunities to unravel the epigenetic landscape of monocytes and provides insights into the immune-mediated mechanisms driving immune-related diseases. Below we highlight several findings from two immune-related diseases.

For Type 2 Diabetes (T2D), we identified 13 overlapped genes associated with T2D in both ancestries (Supplementary Table 4). We pinpointed the most significant genes with smallest p-values: transcription factor 7 like 2 (*TCF7L2*), ankyrin 1 (*ANK1*), fat mass and obesity associated alpha-ketoglutarate dependent dioxygenase (*FTO*), NK6 homeobox 3 (*NKX6-3*), and tyrosin hydroxylase (*TH*). *TCF7L2* association with T2D has been consistently replicated in multiple populations with diverse genetic origins[71] and experimentally validated[72]. Genome-wide association studies have identified *ANK1* as a common T2D susceptibility locus.[73] The other finding suggests that certain variants in *ANK1* could contribute to insulin resistance, a key feature in the development of T2D.[74] *FTO* were reported to be associated with T2D, primarily through their impact on BMI and obesity.[75] *NKX6-3*, along with other specific pancreatic islet β-cell transcription factors, is sensitive to oxidative stress, a condition associated with β-cell dysfunction in both Type 1 and Type 2 diabetes.[76] Some GWAS studies suggest that *TH* gene may play a role in T2D susceptibility and insulin resistance. [77,78]

Additionally, we identified seven genes associated with T2D uniquely in the AA ancestry population (Supplementary Table 3.1). Specifically, we identified *BCKDHA*, which encodes the branched-chain alpha-keto acid (BCAA) dehydrogenase (BCKD) Subunit. BCAA was reported to be elevated in both human and animal model of obesity.[79,80] At the same time, obesity-associated suppression of BCKD complex in liver and adipose tissue was observed.[81] Due to the widespread

medRxiv preprint doi: https://doi.org/10.1101/2024.08.12.24311885; this version posted August 13, 2024. The copyright holder for this preprint (which was not certified by peer review) is the author/funder, who has granted medRxiv a license to display the preprint in perpetuity. All rights reserved. No reuse allowed without permission.

expression of BCKD in different tissues including monocytes, it's worth to study the specific role of BCKD in immune systems in T2D patients.

Coronary Artery Disease (CAD) is a severe cardiovascular condition characterized by the buildup of atherosclerotic plaques in the coronary arteries, leading to reduced blood flow and increased risk of heart attacks.[82] While traditional risk factors contribute to CAD development, emerging evidence suggests a crucial role for the immune system, particularly monocytes.[83] Studies have shown associations between CAD and elevated levels of CD14+CD16+ monocytes, a pro-inflammatory monocyte subtype with potential as a biomarker.[84] In our MWAS results, we identified 130 genes that are associated with CAD in EA ancestry. We pinpointed several genes that are either well-known or act in inflammatory pathway of CAD. The *CDKN2A/B* locus encodes cyclin-dependent kinase inhibitors (p16INK4a and p15INK4b) that regulate cellular senescence and cell cycle progression.[85] Dysregulation of these genes can contribute to aberrant vascular smooth muscle cell proliferation and inflammation, promoting the development and progression of atherosclerotic lesions, a key underlying mechanism in CAD pathogenesis.[86] We also identified *CXCL12* (stromal cell-derived factor-1), which is a chemokine that regulates the migration and homing of various cell types, including inflammatory cells and progenitor cells, through interactions with its cognate receptor, CXCR4.[87,88] Dysregulation of the CXCL12/CXCR4 axis can contribute to the pathogenesis of CAD by modulating monocyte recruitment[89], endothelial progenitor cell function, and neovascularization processes implicated in atherosclerotic plaque formation and vascular remodeling.[88] We also identified *IL6R* (Interleukin 6 Receptor) which mediates the interleukin-6 signaling pathway, is a critical pathway in inflammation and has been implicated in the pathogenesis of CAD.[90] SMAD3 involved in the TGF-beta signaling pathway, which has roles in both immune response and tissue homeostasis.[91] It has been linked to mechanisms that could contribute to atherogenesis.

Notably, our WGBS approach identified substantially more gene-phenotype associations compared to analyses restricted to CpG sites covered by conventional methylation arrays. For the EA population, using only 450K array sites yielded 1,354 associations, with 1,105 overlapping those found in WGBS. Similarly, the 900K array identified 1,929 associations, with 1,644 overlaps. In the AA population, the 450K array detected 136 associations (102 overlaps with WGBS), while the 900K array found 200 associations (153 overlaps). These results underscore the superior coverage of WGBS, revealing numerous associations missed by array-based approaches. For instance, in T2D analysis, array-based methods only identified associations with three genes (TCF7L2, *FTO*, and *KCNC2*), whereas our WGBS approach uncovered several additional genes, as discussed earlier.

In summary, the application of our MWAS has been proven consistent and reliable for studying complex traits. The insights gleaned from our research reveal novel associations between DNAm patterns and phenotype expressions, which are not covered by traditional methylation arrays, highlighting important biological linkages. Specifically, our findings are invaluable for understanding inflammatory diseases in monocytes. These discoveries pave the way for the identification of therapeutic targets that are specific to particular ancestries, with implications for a multitude of complex conditions.

medRxiv preprint doi: https://doi.org/10.1101/2024.08.12.24311885; this version posted August 13, 2024. The copyright holder for this preprint (which was not certified by peer review) is the author/funder, who has granted medRxiv a license to display the preprint in perpetuity. All rights reserved. No reuse allowed without permission.

Concordance with colocalization and MR analysis

We aligned our MWAS findings with insights from Mendelian Randomization (MR)[92] and Bayesian colocalization analyses[93] for AA and EA ancestries separately. We identified 36,292 CpG-phenotype pairs in the EA group and 1,804 in the AA group that exhibited causal relationships as determined by MR, using a stringent Bonferroni-corrected significance threshold of 1.2×10^{-9}. Remarkably, 68.6% (21,483 of 31,334) of MWAS-identified associations for EA and 42.3% (1,270 of 2,998) for AA supported by MR. Specifically, out of the 537 MWAS associations consistently identified across both African and European ancestries, 89.9% (483) supported by MR.

For the Bayesian colocalization analyses, we found that 36.8% of MWAS-identified associations (11,517 out of 31,336) in EA and 9.4% in AA (281 out of 2,998) exhibited strong evidence for colocalization, indicated by a posterior probability (PPH4) exceeding 0.7, suggesting a shared causal variant. Among MWAS associations that are consistently identified across both ancestries, 42.8% (230 out of 537) presented evidence for colocalization, indicating that a substantial proportion of these associations are likely driven by the same causal variants in both populations. (Supplementary Table 2.1 and 2.2)

Identification of *trans*-meQTL for whole genome DNAm sites across two populations

The study identified a substantial number of t*rans*-meQTL associations in both the AA and EA populations, using a conservative threshold of 1×10^{-14}. In the AA population, 1,664,615 *trans*-meQTL associations were detected, involving 159,053 CpG sites (0.6% of all sites tested). In the EA population, 2,484,481 *trans*-meQTL associations were identified, involving 103,768 CpG sites (0.4% of all sites tested). Interestingly, only 1,952 CpG sites with *trans*-meQTL associations overlapped between the two populations and the vast majority of CpG sites with *trans*-meQTL associations were unique to each population, with 98.8% (157,101) of the sites being specific to the AA population and 98.1% (101,816) being specific to the EA population, highlighting the population-specific nature of these associations. On average, each CpG site had 0.06 *trans*-meQTL mappings in the AA population and 0.10 in the EA population, suggesting a slightly higher number of *trans*-meQTL associations per CpG site in the EA population compared to the AA population.

Our analysis of *trans*-meQTL associations across two populations revealed a general negative correlation between MAF and effect size when MAF is greater than 0.05 (AA: coefficient $= -3.0$, $P < 2 \times 10^{-16}$, EA: coefficient $= -2.5$, $P < 2 \times 10^{-16}$). Interestingly, we also observed that variants with extremely low MAFs, around 0.01, exhibited small effect sizes (Fig. 5a). This unexpected pattern may be confounded by the genomic distance between meQTL and CpG sites and warrants further investigation to understand the underlying mechanisms. Further investigation into the relationship between effect size and genomic distance revealed that effect sizes diminish as the distance from the CpG sites increases. Notably, this inverse relationship appears to be more pronounced in the *trans*-meQTL context compared to the *cis*-meQTL findings (Fig. 5b). For *trans*-meQTLs identified in both ancestries, the effect sizes also showed a high degree of concordance (correlation $= 0.97, P < 2 \times 10^{-16}$, Fig. 5c).

medRxiv preprint doi: https://doi.org/10.1101/2024.08.12.24311885; this version posted August 13, 2024. The copyright holder for this preprint (which was not certified by peer review) is the author/funder, who has granted medRxiv a license to display the preprint in perpetuity. All rights reserved. No reuse allowed without permission.

Discussion

We performed whole genome bisulfite sequencing and whole genome sequencing in purified monocytes across 160 and 298 individuals in AA and EA ancestry. We then present a comprehensive analysis of *cis*-genetic regulation of DNAm based on a large discovery study across ancestries. Our study has almost ten times the number of genes with identified *cis*-meQTL associations compared with previous reports[11] and led to understanding of common as well as unique genetic architecture of DNAm in the AA and EA population respectively. We developed models for DNAm imputation separately for the two populations and make them publicly available to facilitate future MWAS. Using large-scale GWAS summary statistics from 41 complex traits in MVP dataset, we illustrate how MWAS can complement GWAS for the identification of causal genes and DNAm and inform potential drug targets.

Our research highlights the importance of considering ancestry when studying the cis-genetic regulation of DNAm, as we have discovered significant differences between populations. We observe that *cis*-h^2 of DNAm levels in AA ancestry is higher than that of EA ancestry (Fig. 3a, d). Further, the CpG sites with higher *cis*-h^2 values tend to correspond to more *cis*-meQTL associations (Fig. 3c). Importantly, we found nearly 30% of the *cis*-meQTL detected in the AA population were nonexistent or rare in the EA population, but the converse proportion was much more modest (~8%). Fine-mapping analysis, conducted separately for each population, revealed that the number of genetic variants potentially responsible for regulating DNAm at CpG sites was considerably lower in the AA population compared to the EA population. Taken together, our analysis demonstrates that there are distinct advantages of including samples from diverse ancestries in genetic studies of DNAm.

Furthermore, we have built comprehensive MWAS models and uncovered new biological insights regarding the influence of DNAm on a spectrum of complex traits and diseases. Notably, many of the identified methylation marker regions were not covered by the conventional 450K/EPIC BeadChip arrays, underlining the pioneering nature of our approach. By mapping these novel marker regions to adjacent genes, we discovered that a number of them play a crucial role in disease pathogenesis through the modulation of protein expression, immune system interactions, and other biological processes. For instance, genes like *TCF7L2* and *FTO*, identified in our study, have established links to Type 2 Diabetes and obesity, aligning with previous genetic and epigenetic research. We have also identified key genes that play crucial roles in the inflammatory pathways involved in coronary artery disease. Furthermore, our analysis highlighted genes like *BCKDHA* that are unique to the African ancestry cohort, presenting opportunities for the development of ancestry-specific treatments and interventions.

A recent study[94] has established that the DNAm landscape is predominantly shaped by cell types and cell-type-specific regulatory programs. Extending beyond these findings, our study demonstrates that at least some DNAm is also tightly influenced by genetic factors, even within a homogeneous cell type such as monocytes. These two findings are not contradictory but complementary, as they highlight different layers of DNAm regulation: cell-type-specific programs provide the broad framework, while genetic factors fine-tune DNAm patterns within that framework. This discovery significantly expands our understanding of the genetic architecture of DNAm,

medRxiv preprint doi: https://doi.org/10.1101/2024.08.12.24311885; this version posted August 13, 2024. The copyright holder for this preprint (which was not certified by peer review) is the author/funder, who has granted medRxiv a license to display the preprint in perpetuity. All rights reserved. No reuse allowed without permission.

suggesting a complex interplay between genetic inheritance and epigenetic regulation within monocytes. In the future, it would be interesting to investigate how nongenetic factors shape the DNAm landscape and relate to phenotypes. Additionally, future studies should consider jointly analyzing the transcriptome and methylome to gain a more comprehensive understanding of the complex regulatory mechanisms at play.

We conclude by discussing several limitations in our study. First, the current sample size is relatively small, particularly for the AA cohort, which consisted of only 160 individuals, compared to 298 in the EA group. However, it is important to note that our study is still one of the largest studies to date, especially for the comparison of EA and AA populations. This disparity in sample sizes has implications for the robustness and interpretability of our findings. As previously discussed, the smaller sample size in the AA population may have led to an underestimation of the number of *cis*-meQTL associations. Also, the *trans*-regional effects of DNAm, which involve interactions between genetic variations and CpG sites across different genomic regions, require large sample sizes to detect due to their typically smaller effect sizes and the complex nature of their interactions.[95] Second, our samples come from Tulane cohort are exclusively males and the samples in MVP are approximately 90% males. While DNAm patterns have been shown to be relatively consistent between genders[96], subtle differences may still exist.[97] Third, our study focused on WGBS sequencing in purified monocytes, providing a valuable starting point for exploring epigenetic mechanisms in a specific cell type. By focusing on monocytes, we have laid a foundation for future studies to expand upon and explore DNAm patterns in other cell types. This approach will enable a more comprehensive understanding of the epigenetic landscape across various tissues and cell populations, ultimately contributing to a holistic view of the role of DNAm in health and disease.

medRxiv preprint doi: https://doi.org/10.1101/2024.08.12.24311885; this version posted August 13, 2024. The copyright holder for this preprint (which was not certified by peer review) is the author/funder, who has granted medRxiv a license to display the preprint in perpetuity.
All rights reserved. No reuse allowed without permission.

Figures

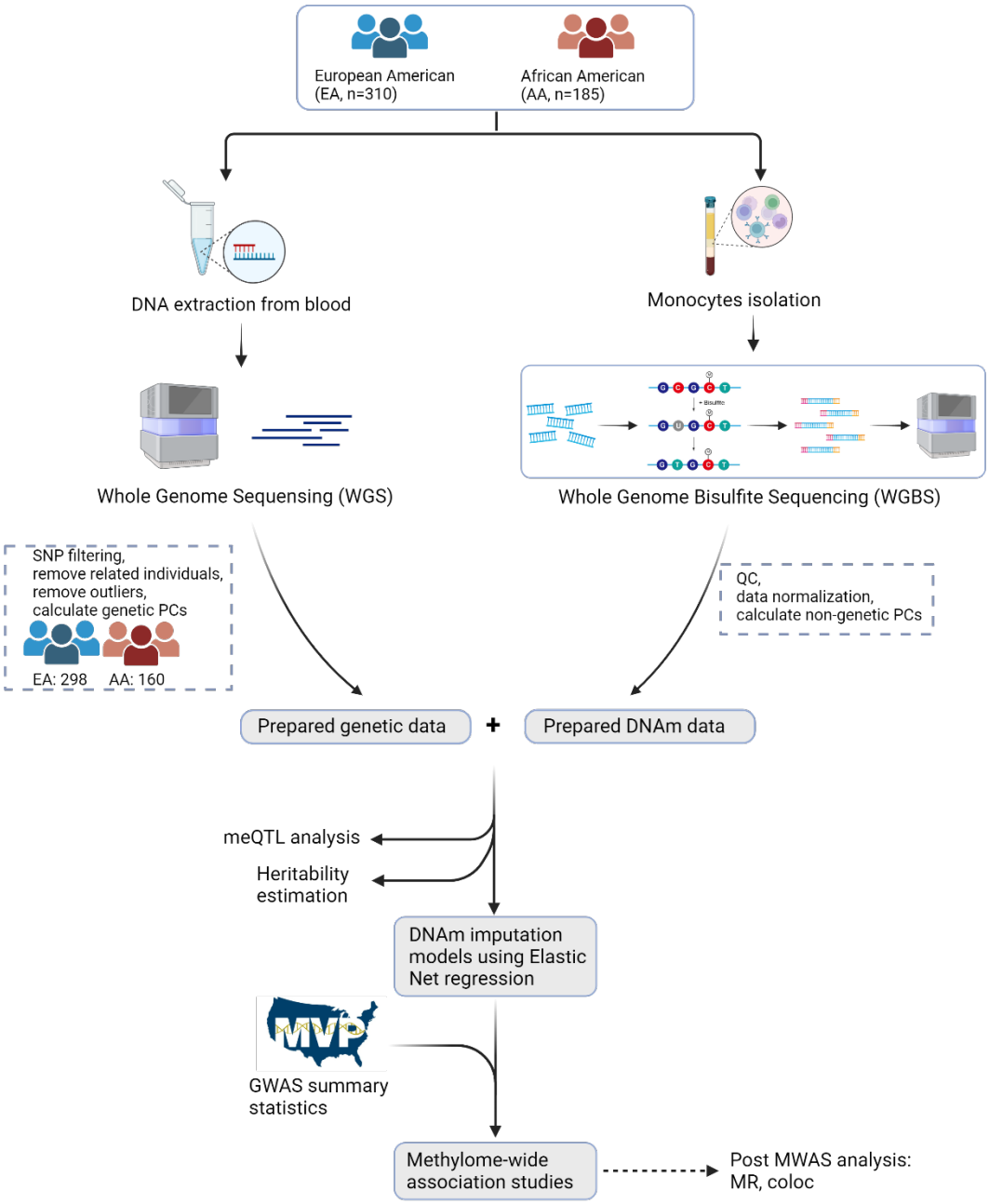

Fig.1 Overview of the data collection, preparation, and analysis pipeline.

medRxiv preprint doi: https://doi.org/10.1101/2024.08.12.24311885; this version posted August 13, 2024. The copyright holder for this preprint (which was not certified by peer review) is the author/funder, who has granted medRxiv a license to display the preprint in perpetuity. All rights reserved. No reuse allowed without permission.

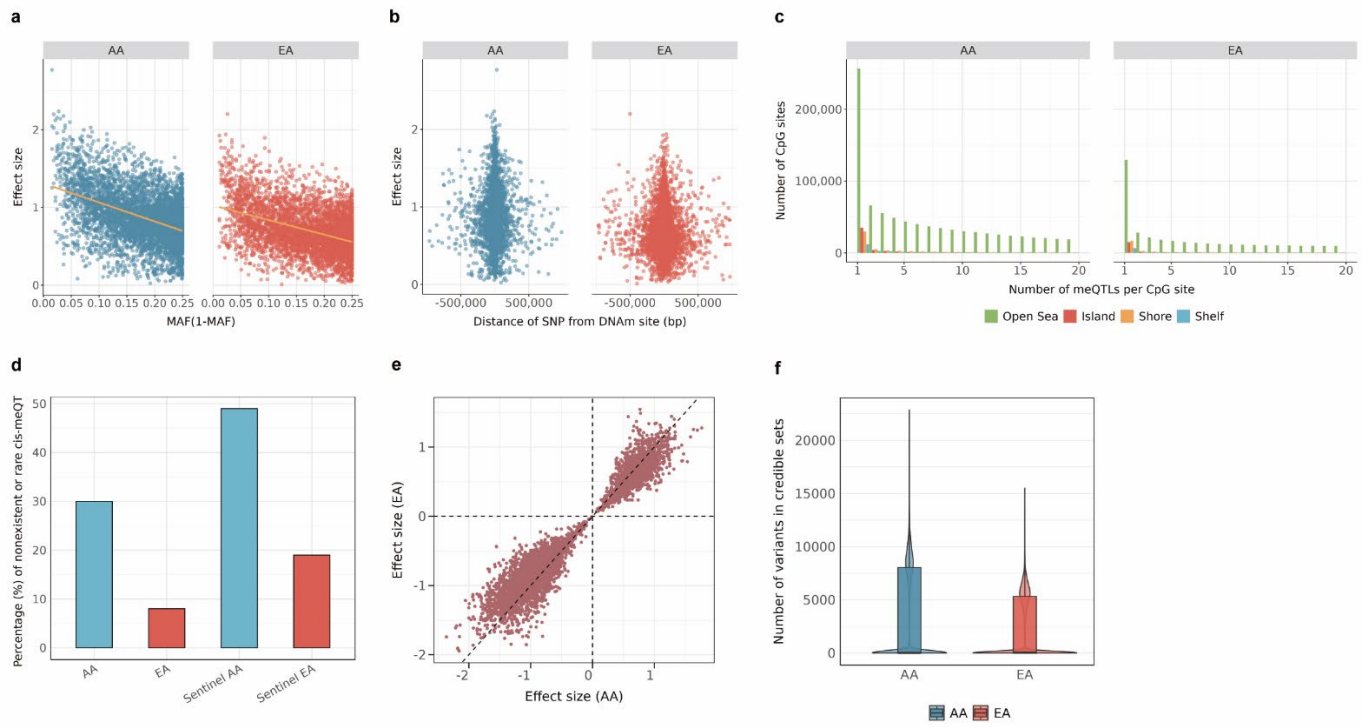

Fig.2 *cis*-meQTL and fine-mapping analysis across AA and EA populations. a, Effect sizes of *cis*-SNPs of meQTL versus minor allele frequencies (MAF(1-MAF)). The orange regression line indicates the trend across the dataset. **b**, shows the effect size in relation to the distance from SNP to DNAm site for the AA (left) and EA (right) groups. The distance are measured in base pairs (bp). **c**, Distribution of CpG sites by number of associated *cis*-meQTLs in AA and EA ancestries. The bar chart categorizes CpG sites based on the number of *cis*-meQTLs identified, with annotations for four genomic regions: CpG islands, which are regions with a high CpG density; CpG shores, located within 2 kb of islands; CpG shelves, extending an additional 2 kb from shores; and Open Sea, which represents areas more distal to the islands, shores, and shelves. Each region is color-coded. **d**, Percentage of nonexistent or rare *cis*-meQTLs across ancestries. It displays the proportion of identified *cis*-meQTLs that are absent or rare within the contrasting population from the 1000 Genomes Project. The four bars represent *cis*-meQTL associations for AA, EA, sentinel *cis*-meQTLs for AA and EA, respectively. Sentinel *cis*-meQTL is defined as the most significant SNPs for each CpG site. **e**, illustrates the effect size of *cis*-meQTL in AA ancestry compared to EA ancestry. **f**, Distributions of size of credible sets in SuSIE across CpG sites that have at least one significant *cis*-meQTL in both AA and EA ancestries. Boxes are drawn from first and third quartiles, with the median at the center, and the whiskers extending to 1.5 times the interquartile range from the box boundaries. The width of the violin at a particular point represents the density of data points at that value.

medRxiv preprint doi: https://doi.org/10.1101/2024.08.12.24311885; this version posted August 13, 2024. The copyright holder for this preprint (which was not certified by peer review) is the author/funder, who has granted medRxiv a license to display the preprint in perpetuity. All rights reserved. No reuse allowed without permission.

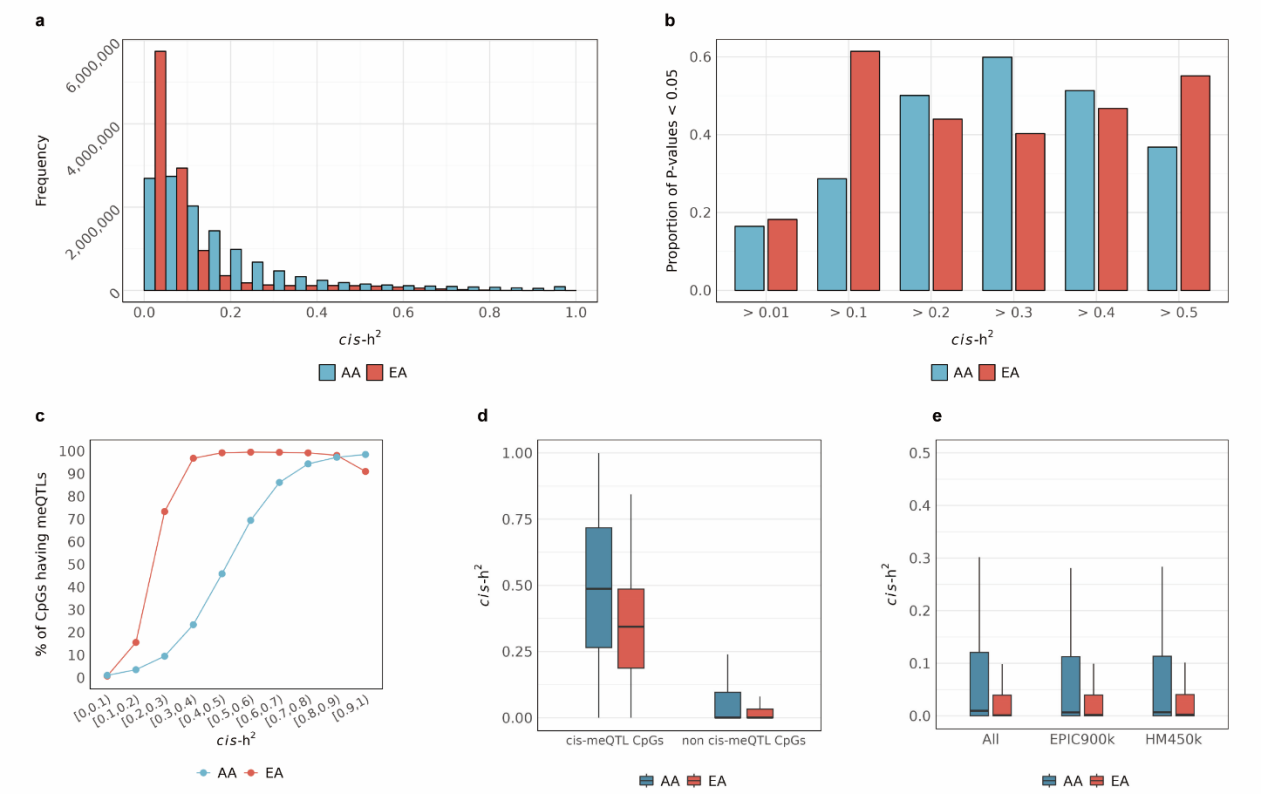

Fig.3 *cis*-h^2. a, The distribution of *cis*-heritability estimates for CpG sites with *cis*-h^2> 0.01. **b**, illustrates the proportions of having p-values smaller than 0.05 among the CpG sites with *cis*-h^2 greater than a cutoff. **c**, Relationship between *cis*-heritability and the percentage of CpG sites with *cis*-meQTL associations in AA and EA ancestries. **d**, displays the distribution of cis-heritability estimates for all CpG sites, CpG sites with at least one *cis*-meQTL, and CpG sites without *cis*-meQTL associations in AA and EA ancestries. **e**, displays the distribution of *cis*-h^2 for all CpG sites, CpG sites contains in EPIC850K and CpG sites contains in HM450K. Boxes in c and d are drawn from dirst and third quartiles, with the median at the center, and the whiskers extending to 1.5 times the interquartile range from the quartiles.

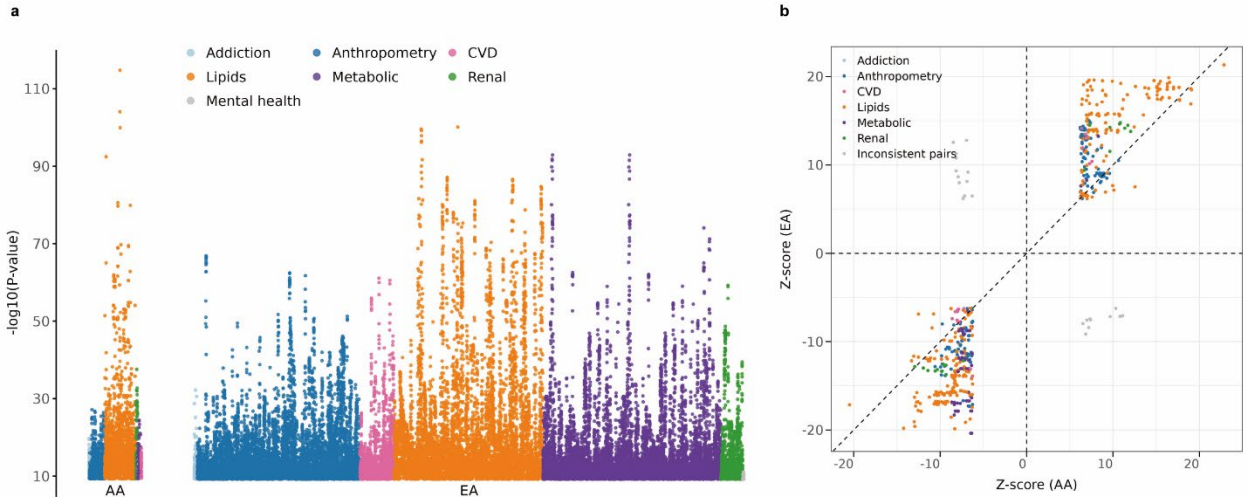

medRxiv preprint doi: https://doi.org/10.1101/2024.08.12.24311885; this version posted August 13, 2024. The copyright holder for this preprint (which was not certified by peer review) is the author/funder, who has granted medRxiv a license to display the preprint in perpetuity. All rights reserved. No reuse allowed without permission.

Fig.4 MWAS results for 41 phenotypes in the MVP dataset. **a**, demonstrates the significant MWAS associations after Bonferroni correction (P cutoff is 4.9×10^{-10} for AA and 6.6×10^{-10} for EA). Different categories of traits are labeled with different colors. **b,** illustrates the consistency of Z-scores for associations that were significant in both AA and EA ancestries. Each dot represents a CpG-phenotype pair that was found significant in both ancestries. CpG-phenotype pairs with inconsistent directions are marked in grey and those with consistent directions are marked in colors for different categories.

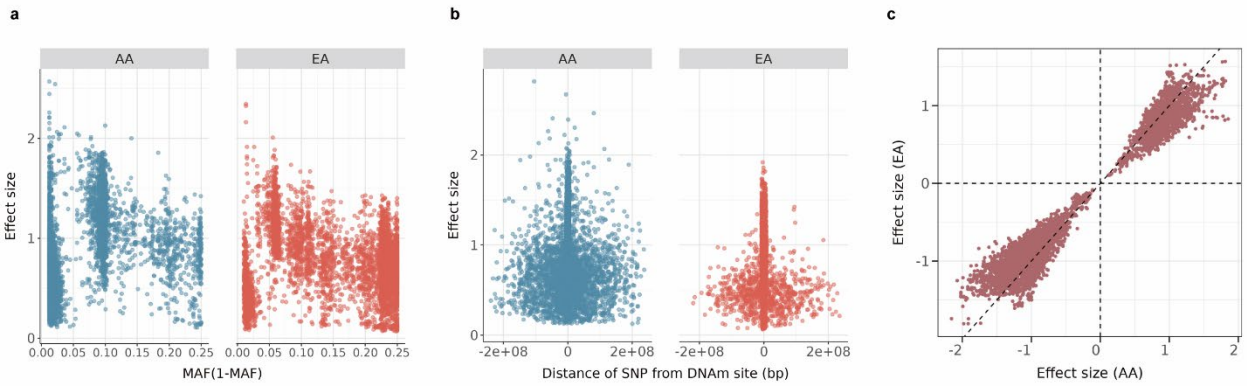

Fig.5 *Trans*-meQTL analysis. a, Effect sizes of *trans*-SNPs of meQTL versus minor allele frequencies (MAF(1-MAF)). The orange regression line indicates the trend across the dataset. **b,** shows the effect size in relation to the distance from SNP to DNAm site for the AA (left) and EA (right) groups. The distance is measured in base pairs (bp). **c,** illustrates the effect size of *trans*-meQTL in AA ancestry compared to EA ancestry.

medRxiv preprint doi: https://doi.org/10.1101/2024.08.12.24311885; this version posted August 13, 2024. The copyright holder for this preprint (which was not certified by peer review) is the author/funder, who has granted medRxiv a license to display the preprint in perpetuity. All rights reserved. No reuse allowed without permission.

Methods

Study subjects

We recruited a total of 495 male subjects, aged 37.2 ± 8.8 years (mean ± SD), from our ongoing Tulane Louisiana Osteoporosis Study cohort. The study population consisted of 310 (62.6%) self-identified EA and 185 (37.4%) AA. The mean height and weight of the subjects were 175.8 ± 7.1 cm and 83.4 ± 16.2 kg, respectively. Within the cohort, 355 (71.7%) subjects reported smoking, 342 (69.1%) reported alcohol consumption, and 368 (74.3%) reported regular exercise. The racial/ethnic composition and lifestyle factors were representative of the general population in the study area (Supplementary Table 1).

We excluded individuals with preexisting conditions relevant to bone mass development and immune system, including: (1) cerebral vascular disease, (2) diabetes mellitus, except for easily controlled, noninsulin dependent cases, (3) chronic renal or liver failure, (4) chronic lung disease, (5) chronic obstructive pulmonary disease, (6) any metabolic or inherited bone diseases (e.g., hyper/hypoparathyroidism, Paget's disease, osteomalacia, osteogenesis imperfecta, and hypochondrogenesis), (7) collagen disorder (e.g., rheumatoid arthritis, except for minor cases that involve only hand joint and wrist), (8) chronic gastrointestinal disease, (9) alcohol abuses, (10) treatment with corticosteroid or anticonvulsant therapy for more than 6 months duration, (11) antibiotic usage, (12) gastroenteritis, (13) major surgeries, (14) intercontinental travel in the past 3 months, (15) autoimmune or autoimmune-related diseases (e.g., multiple sclerosis), (16) immune-deficiency conditions (e.g., HIV infection), (17) haematopoietic and lymphoreticular malignancies (e.g., leukaemias), (18) active periods of asthma, or (19) influenza, infected within one week of recruitment. All qualified individuals signed an informed consent document before any data and biosample collection. The study was approved by the Tulane University Institutional Review Board (IRB #: 10-184088).

Whole Genome Sequencing (WGS)

DNA for WGS was extracted from the blood using the Gentra Puregene Blood Kit (Qiagen, USA). Concentration and quality of all the extracted DNA were assessed using Nanodrop 1000 and the samples were kept at -80 °C until further use. Briefly, 300 ng genomic DNA was used as input. The workflow for library preparation consists of DNA Nanoballs (DNBs) generation through ligation-mediated polymerase chain reaction (LM-PCR), single-strand separation, cyclization, and rolling circle amplification procedures. Two sequencing depths were utilized for this study: 130 samples were sequenced to an average depth of 22x, while another subset was sequenced to an average depth of 15x. The WGS was conducted using DNBSEQ-500^{TM} sequencing technology platform (BGI Americans Corporation, Cambridge, MA, USA), with 350 bp paired-end reads in length. Each sample's cleaned and aligned data was mapped to the human reference genome (GRCh38/hg38) using Burrows-Wheeler Aligner (BWA, v0.7.12) software[98]. For accurate variant calling, we adhered to the recommended Best Practices ,for variant analysis using the Genome Analysis Toolkit (GATK, v4.0.3)[99,100]. HaplotypeCaller of GATK was employed to identify genomic variations, and the variant quality score recalibration (VQSR) was applied to obtain high-confident variant calls.[99,100]

medRxiv preprint doi: https://doi.org/10.1101/2024.08.12.24311885; this version posted August 13, 2024. The copyright holder for this preprint (which was not certified by peer review) is the author/funder, who has granted medRxiv a license to display the preprint in perpetuity. All rights reserved. No reuse allowed without permission.

Isolation of Monocytes, their Genomic DNA, and Total RNA

In the present study, we focused specifically on peripheral blood monocytes (PBMs), which can act as osteoclast precursors and play important roles in regulating bone metabolism.[101] Briefly, peripheral blood mononuclear cells (PBMCs) were firstly separated from ~60 ml freshly collected peripheral blood, by a density gradient centrifugation method using Histopaque-1077 (Sigma-Aldrich, USA). The PBMCs were washed repeatedly with 2 mM EDTA in PBS, before being dissolved in 0.5% BSA and 2 mM EDTA in PBS. PBMs were then isolated from the PBMCs with a Monocyte Isolation Kit II (Miltenyi Biotec Gmbh, Bergisch Glagbach, Germany) according to the manufacturer's protocol. The kit depleted unwanted cells (such as T and B cells) from PBMCs, leaving PBMs free of the surface-bound antibody and beads with minimum disturbance. The isolated PBMs were visually checked for purity and counted under microscope. The genomic DNA used for WGBS and total RNA used for RNA-seq were extracted from the freshly isolated PBMs with the AllPrep DNA/RNA/miRNA Universal Kit (Qiagen, USA) following the manufacturer's protocol and kept at -80 °C until further use.

Whole Genome Bisulfite Sequencing (WGBS)

DNAm profiles were determined by WGBS according to previously published protocols.[102] Briefly, 100 ng genomic DNA isolated from PBMs was fragmented by sonication using a Bioruptor (Diagenode, Belgium) to a mean size of approximately 250 bp, followed by the blunt-ending, dA addition to 3'-end, and adaptor ligation. The ligated libraries were bisulfite converted using the EZ DNA Methylation-Gold kit (Zymo Research Corp, USA). The WGBS was conducted on DNAs extracted from isolated PBMs at an average read depth of 20x using HighSeq 4000 Illumina platform (BGI Americans Corporation, Cambridge, MA, USA).

Data filtering includes removing adaptor sequences, contamination, and low-quality reads from raw reads. Raw reads were also excluded if the number of unknown bases exceeded 10% or if the ratio of bases with a quality score less than 20 exceeded 10%, in order to obtain high-quality and cleaned data. The cleaned and aligned data was mapped to the human reference genome (GRCh37/hg19) using BSMAP[103], which was later converted to GRCh38/hg38 using UCSC LiftOver tool (https://genome.ucsc.edu/cgi-bin/hgLiftOver). The methylation level of a CpG dinucleotide was determined by the ratio of the number of methylated reads to the total number of reads covering a particular cytosine site.

Bulk transcriptomics (RNA-seq) and cell deconvolution

For the RNA sequencing experiment, RNA integrity was assessed using the Agilent Technologies 2100 Bioanalyzer. Libraries for RNA-seq were prepared following Illumina's TruSeq-stranded-total-RNA-sample preparation. Briefly, 500 ng RNA was used as input. The workflow consists of rRNA removal, cDNA generation, and end repair to generate blunt ends, A-tailing, adaptor ligation and PCR amplification. The libraries were pooled and diluted to 2 nM in EB buffer and then denatured using the Illumina protocol. The denatured libraries were diluted to 10 pM by pre-chilled hybridization buffer and loaded onto Illumina NovaSeq 6000 sequencing system (LC Sciences, Hangzhou, China) using a paired-read recipe according to the manufacturer's instructions.

medRxiv preprint doi: https://doi.org/10.1101/2024.08.12.24311885; this version posted August 13, 2024. The copyright holder for this preprint (which was not certified by peer review) is the author/funder, who has granted medRxiv a license to display the preprint in perpetuity. All rights reserved. No reuse allowed without permission.

Quality control analysis and quantification of the sequencing library were performed using Agilent Technologies 2100 Bioanalyzer High Sensitivity DNA Chip. Paired-ended sequencing was performed. Cutadapt[104] was used to remove the reads that contained adaptor contamination, low quality bases, and undetermined bases. The sequence quality was verified using FastQC (http://www.bioinformatics.babraham.ac.uk/projects/fastqc/). Bowtie2[105] and HISAT2[106] were used to map read to the genome of *Homo sapiens* (v96; GRCh38/hg38). The mapped reads of each sample were assembled using StringTie[107]. Then, all transcriptomes from the samples were merged to reconstruct a comprehensive transcriptome using perl scripts and gffcompare (https://github.com/gpertea/gffcompare/). After the final transcriptome was generated, StringTie was used to estimate the expression levels of all transcripts in transcripts per million (TPM).[107]

Cell deconvolution analysis was conducted using the Estimated the Proportion of Immune and Cancer (EPIC v1.1.7)[108], which utilized its embedded circulating immune cells (BRef) as the reference profile to estimate the fraction of mRNA contribution to the bulk by each cell type. The reference profile, purified from PBMs or whole blood, includes B cells, CD4+ T cells, CD8+ T cells, monocytes, neutrophils, and natural killer cells. In addition to the default list of signature genes, 10 additional user-selected cell marker genes were incorporated to enhance the deconvolution of cell proportions by EPIC. These added cell marker genes are *CD3D/E/G*, *CD4*, *CD8A*, *CD14*, *CD19*, *CD86*, and *FCGR3A/B*.

Data preparation

Genotype data

We followed the GoDMC pipeline[109] for the genotype data processing. Each study performed quality control on genotype data for chromosomes 1-22. SNPs that failed the Hardy-Weinburg equilibrium ($P < 10^{-6}$), and had an MAF < 0.01 were removed. Then we removed the duplicated SNPs and SNPs with mismatched alleles and recoded indel alleles to I and D. Next, we calculated the first 10 genetic PCs on the SNPs extracted from HapMap3 SNPs without long-range linkage disequilibrium (LD) (MAF > 0.2). Ancestry outliers that deviated by 7 s.d. from the mean were removed. After outlier removal, we recalculated genetic PCs for use in subsequent analyses. To identify relatedness in unrelated datasets, we calculated genome-wide average identity by state using PLINK1.90. Participants with identity by state > 0.125 were removed. As a result, we had 160 and 298 samples left in AA and EA, respectively.

DNAm data normalization

To transform our DNAm data into a distribution that more closely approximates a Gaussian distribution, we applied a rank-based inverse normal transformation (INT)[50]. This method comprised two steps. In the first, the observations are transformed onto the probability scale using the empirical cumulative distribution function (ECDF). In the second, the observations are transformed onto the real line, as Z-scores, using the probit function.

Co-variates

We used age, BMI, smoking, alcohol consumption, proportion of blood cells with most variation (B cells, monocytes, neutrophils), and 10 genetic PCs as well as 10 nongenetic PCs to adjust for

medRxiv preprint doi: https://doi.org/10.1101/2024.08.12.24311885; this version posted August 13, 2024. The copyright holder for this preprint (which was not certified by peer review) is the author/funder, who has granted medRxiv a license to display the preprint in perpetuity. All rights reserved. No reuse allowed without permission.

possible confounding. To achieve the nongenetic principal components, we performed a PCA on the 20,000 most variable DNAm sites and selected the first 10 PCs.

meQTL analyses

We performed a comprehensive analysis of all *cis*- and *trans*-meQTL mappings using the MatrixEQTL[52] package in R on 25 million normalized DNAm sites in African (n = 160) and European (n = 298) ancestries, separately. We defined the *cis*-regions to be within ±1 Mb of the CpG sites. The DNAm data was firstly regressed out the covariates defined in the previous section. Then, for each DNAm CpG sites j, the residual value, y_{ji}, was regressed against each SNP k:

$$y_{ji} = \alpha_{jk} + \beta_{jk} x_{ki} + \epsilon_{jki}$$

where genotype values x_{ki} were standardized to have a mean of zero and a standard deviation of one, α_{jk} was the intercept term, and β_{jk} was the effect estimate of each SNP k on each residualized CpG site j. We used 1×10^{-8} as the p-value cutoff for identification of significant *cis*-meQTL mappings and used 1×10^{-14} for *trans*-meQTL mappings.

Fine-mapping

To ascertain the potentially causal variants influencing DNAm, we conducted fine-mapping on *cis*-SNPs associated with each CpG site. This was specifically focused on 12,706,905 and 11,041,146 CpG sites linked with at least one *cis*-meQTL in AA and EA populations, respectively. Utilizing SuSiE[57] from susieR package in R for this analysis, we were able to deduce single effect components or credible sets for each CpG site and its corresponding variants. These credible sets carry a 95% likelihood of encompassing at least one variant exerting a nonzero causal impact. We limited the number of credible sets to a maximum of ten (L = 10), which is based on the hypothesis that up to ten variants could potentially regulate a single CpG site.

***Cis*-h^2**

We employed Genome-wide Complex Trait Analysis[58] (GCTA, version 15) to estimate the h^2 – the proportion of phenotypic variance attributable to genetic factors – for each CpG site among the total of 25 million analyzed. This estimation was performed using SNPs exclusively from *cis*-regions. GCTA operates by constructing a genetic relationship matrix (GRM) from SNP data, which encapsulates the degree of genetic similarity between pairs of individuals in the study. We then utilized this GRM within a restricted maximum likelihood (REML) analysis framework to estimate h^2. This approach allows for the separation of the phenotypic variance into components attributed to genetic variance (captured by the SNPs in the *cis*-regions) and residual variance. By focusing on *cis*-regional SNPs, our analysis specifically targets the genetic contribution to DNAm variance at each CpG site, providing insights into the genetic underpinnings of epigenetic modifications. To validate and enhance the robustness of our results, we also conducted a comparative analysis of the *cis*-h^2 of CpG sites within our WGBS dataset against those listed from two platforms: MethylationEPIC Infinium v2.0 that covers over 935,000 CpG methylation sites[59] (900K) and Infinium HumanMethylation450 Beadchip[60] (450K).

DNAm imputation model

In our study, we focused on CpG sites exhibiting a *cis*-h^2 threshold above 0.01 and associated with a minimum of 10 *cis*-SNPs. A 500-kp window was adopted around each target CpG site to

medRxiv preprint doi: https://doi.org/10.1101/2024.08.12.24311885; this version posted August 13, 2024. The copyright holder for this preprint (which was not certified by peer review) is the author/funder, who has granted medRxiv a license to display the preprint in perpetuity. All rights reserved. No reuse allowed without permission.

enhance computational efficiency during model training. For the genotype data, following others[68,110], we omitted SNPs with a MAF under 1%, SNPs with ambiguous strand orientation, those containing insertions or deletions, and SNPs absent in the LD reference panel derived from the 1000 Genomes Project[56]. Our DNAm imputation model was constructed using a penalized regression approach, integrating methylation and genotype data within the defined *cis*-regions. Let Y be the n-dimensional vector representing the methylation data for a particular CpG site, and let $\boldsymbol{X}$ be the $n \times k$ matrix representing the genotype data for k *cis*-SNPs associated with this CpG site:

$$Y = \boldsymbol{X}w + \varepsilon$$

where w is a $k \times 1$ vector of effect size to be estimated, and ε is the random noise with a mean of zero. The objective function $f(w)$ for a penalized regression to estimate w is:

$$f(w) = \frac{(Y - \boldsymbol{X}w)'(Y - \boldsymbol{X}w)}{N} + J_\lambda(w)$$

where $J_\lambda(w)$ represents a penalty term that regularizes the coefficients to prevent overfitting. Here, we used Elastic-net[64] penalty, which combined both L1 and L2 regularization terms:

$$J_\lambda(w) = \lambda(\alpha \sum |w_j| + \frac{1-\alpha}{2} \sum w_j^2)$$

where λ is the tuning parameter that controls the overall strength of the penalty, α is the elastic-net mixing parameter, which is 0.5 in this study, that determines the trade-off between L1 penalty (lasso) and L2 penalty (ridge). λ is chosen via cross-validation.

The performance of the imputation models was evaluated by predictive R^2, the squared Pearson correlation coefficient between genetically predicted and directly measured DNAm data in nested cross validation[111]. We only considered models with R^2 greater than 0.01 and had a corresponding set of more than 10 *cis*-acting SNPs in the subsequent analysis[47].

MWAS association testing in MVP database

In this section we would like to test the association between predicted methylation levels and trait of interest. In our study, when only summary-level GWAS data of phenotypes were available, we adopted the methodology outlined in existing studies[112,113] to mitigate the discrepancies that often arise from employing LD matrices from reference panels, which may not accurately reflect the LD structure inherent in the GWAS data. In our MWAS association test, we estimated the effect size $\hat{\gamma}$ and its variance between the DNAm and phenotype by:

$\hat{\gamma} = \frac{\hat{w}'Z/\sqrt{n_s}}{\sigma_r}$ and $\widehat{Var}(\hat{\gamma}) = \left(\frac{1}{n_s} + \frac{1}{n_r}\right)\hat{\gamma}^2 + \frac{\zeta^2}{n_s \sigma_r}$

Where Z is the vectors of z-scores from GWAS, $\hat{w}$ is the estimated weights from the DNAm imputation model, n_s is the sample size of the GWAS data, $\sigma_r = \frac{(G_r\hat{w})'(G_r\hat{w})}{n_r}$, $\zeta^2 = 1 - \frac{2\hat{w}'Z\hat{\gamma}}{\sqrt{n_s}} + \sigma_r\hat{\gamma}^2$, G_r is the standardized genotype matrix of the population reference panel, and n_r is the sample size.

We performed this MWAS analysis to 41 phenotypes in the MVP[49] database where GWAS summary statistics were available for both African and European ancestries. Supplementary Table 5 summarized the information of these GWAS summary statistics. In summary, the MVP GWAS summary statistics were obtained from dbGaP (study accession: phs001672.v3.p1). Prior to conducting association tests, we implemented quality control on GWAS summary statistics.

medRxiv preprint doi: https://doi.org/10.1101/2024.08.12.24311885; this version posted August 13, 2024. The copyright holder for this preprint (which was not certified by peer review) is the author/funder, who has granted medRxiv a license to display the preprint in perpetuity. All rights reserved. No reuse allowed without permission.

These included the exclusion of duplicate records, verification and correction of strand orientation for alleles, and the removal of ambiguous alleles, ensuring the integrity and reliability of our association analysis. We also excluded the CpG sites with the number of non-zero weights from DNAm imputation models smaller than 10 to ensure the reliability of the study.

Post-MWAS analyses

We compared our MWAS results with MR analysis in line with the methodology outlined by Zhao, et al.[114]. We selected a set of *cis*-meQTLs as the MR instrumental variables. We first restricted our analysis to the common set of variants that were shared by *cis*-meQTLs and GWAS summary statistics. To avoid the potential issue of collinearity, we removed *cis*-meQTLs strongly correlated with index genetic variants ($r^2 > 0.001$) by applying LD clumping. Then we excluded those who are not significant ($P > 10^{-8}$) *cis*-meQTLs. Second, we applied the Steiger filter[115] to exclude instrumental variables with potential reverse causality. After selecting the instrumental variables, we applied either the Wald ratio (when only one instrumental variable was available) or inverse variance weighting[116] to test the causal link between DNAm and phenotype.

We also conducted Bayesian colocalization analyses[93] on the significant CpG sites identified in our MWAS and MR analysis to estimate the posterior probability that the protein and phenotype shared the same causal variant, using summary-level *cis*-pQTLs and GWAS data. Specifically, we used the coloc R package (v5.2.2), with its default setups in the coloc function, to estimate the posterior probability of both protein and phenotype being influenced by the same causal variant (i.e., the PPH4). We chose PPH4 > 0.7 as the threshold. DNAm satisfying this threshold would suggest a shared causal variant for the *cis*-meQTLs and GWAS associations.

ACKNOWLEDGEMENTS

This work is partially supported by grants from the NIH (U19AG055373, R01AG061917, R01AR069055, P20GM109036, R01CA263494). The content is solely the responsibility of the authors and does not necessarily represent the official views of the National Institutes of Health.

medRxiv preprint doi: https://doi.org/10.1101/2024.08.12.24311885; this version posted August 13, 2024. The copyright holder for this preprint (which was not certified by peer review) is the author/funder, who has granted medRxiv a license to display the preprint in perpetuity. All rights reserved. No reuse allowed without permission.

References

1. Buniello, A. *et al*. The NHGRI-EBI GWAS Catalog of published genome-wide association studies, targeted arrays and summary statistics 2019. *Nucleic Acids Res*. **47**, D1005–D1012 (2019).
2. The GTEx Consortium *et al*. The GTEx Consortium atlas of genetic regulatory effects across human tissues. *Science* **369**, 1318–1330 (2020).
3. Sun, B. B. *et al*. Plasma proteomic associations with genetics and health in the UK Biobank. *Nature* **622**, 329–338 (2023).
4. Liggett, S. B. *et al*. A polymorphism within a conserved β_1-adrenergic receptor motif alters cardiac function and β-blocker response in human heart failure. *Proc. Natl. Acad. Sci*. **103**, 11288–11293 (2006).
5. Olivier, M., Asmis, R., Hawkins, G. A., Howard, T. D. & Cox, L. A. The need for multi-omics biomarker signatures in precision medicine. *Int. J. Mol. Sci*. **20**, 4781 (2019).
6. Jones, P. A. Functions of DNA methylation: islands, start sites, gene bodies and beyond. *Nat. Rev. Genet*. **13**, 484–492 (2012).
7. Unnikrishnan, A. *et al*. The role of DNA methylation in epigenetics of aging. *Pharmacol. Ther*. **195**, 172–185 (2019).
8. Lu, A. T. *et al*. DNA methylation GrimAge strongly predicts lifespan and healthspan. *Aging* **11**, 303 (2019).
9. Marioni, R. E. *et al*. DNA methylation age of blood predicts all-cause mortality in later life. *Genome Biol*. **16**, 25 (2015).

medRxiv preprint doi: https://doi.org/10.1101/2024.08.12.24311885; this version posted August 13, 2024. The copyright holder for this preprint (which was not certified by peer review) is the author/funder, who has granted medRxiv a license to display the preprint in perpetuity. All rights reserved. No reuse allowed without permission.

10. Schübeler, D. Function and information content of DNA methylation. *Nature* **517**, 321–326 (2015).

11. Min, J. L. *et al*. Genomic and phenotypic insights from an atlas of genetic effects on DNA methylation. *Nat. Genet*. **53**, 1311–1321 (2021).

12. Feingold, E. A. *et al*. The ENCODE (ENCyclopedia of DNA elements) project. *Science* **306**, 636–640 (2004).

13. Bernstein, B. E. *et al*. The NIH roadmap epigenomics mapping consortium. *Nat. Biotechnol*. **28**, 1045–1048 (2010).

14. Stunnenberg, H. G. *et al*. The International Human Epigenome Consortium: a blueprint for scientific collaboration and discovery. *Cell* **167**, 1145–1149 (2016).

15. Moss, J. *et al*. Comprehensive human cell-type methylation atlas reveals origins of circulating cell-free DNA in health and disease. *Nat. Commun*. **9**, 5068 (2018).

16. Investigators, A. The atherosclerosis risk in communit (ARIC) study: design and objectives. *Am. J. Epidemiol*. **129**, 687–702 (1989).

17. Dawber, T. R., Meadors, G. F. & Moore, F. E. Epidemiological Approaches to Heart Disease: The Framingham Study. *Am. J. Public Health Nations Health* **41**, 279–286 (1951).

18. Shang, L. *et al*. meQTL mapping in the GENOA study reveals genetic determinants of DNA methylation in African Americans. *Nat. Commun*. **14**, 2711 (2023).

19. Darrell 1, C. G. A. R. N. T. source sites: D. U. M. S. M. R. 1 F. A. 2 B., J. 3 4 5, E. U. V. M. E. G. 3 4 5 B. D. J. 5 6 M. M. G. 3 O. J., Norman 8, H. F. H. M. T. 7 L., Oliver 11, M. A. C. C. A. K. 9 A. Y. W. 10 B. & Michael 13, U. of C. S. F. V. S. 12 B. M. 13 P. Comprehensive genomic

medRxiv preprint doi: https://doi.org/10.1101/2024.08.12.24311885; this version posted August 13, 2024. The copyright holder for this preprint (which was not certified by peer review) is the author/funder, who has granted medRxiv a license to display the preprint in perpetuity. All rights reserved. No reuse allowed without permission.

characterization defines human glioblastoma genes and core pathways. *Nature* **455**, 1061–1068 (2008).

20. Pidsley, R. *et al.* Critical evaluation of the Illumina MethylationEPIC BeadChip microarray for whole-genome DNA methylation profiling. *Genome Biol.* **17**, 208 (2016).
21. de Moura, M. C. *et al.* Epigenome-wide association study of COVID-19 severity with respiratory failure. *EBioMedicine* **66**, (2021).
22. Chu, A. Y. *et al.* Epigenome-wide association studies identify DNA methylation associated with kidney function. *Nat. Commun.* **8**, 1286 (2017).
23. Zillich, L. *et al.* Epigenome-wide association study of alcohol use disorder in five brain regions. *Neuropsychopharmacology* **47**, 832–839 (2022).
24. Barbu, M. C. *et al.* Methylome-wide association study of antidepressant use in Generation Scotland and the Netherlands Twin Register implicates the innate immune system. *Mol. Psychiatry* **27**, 1647–1657 (2022).
25. Huan, T. *et al.* Genome-wide identification of DNA methylation QTLs in whole blood highlights pathways for cardiovascular disease. *Nat. Commun.* **10**, 4267 (2019).
26. Bonder, M. J. *et al.* Disease variants alter transcription factor levels and methylation of their binding sites. *Nat. Genet.* **49**, 131–138 (2017).
27. Lin, H. *et al.* Methylome-wide association study of atrial fibrillation in Framingham Heart Study. *Sci. Rep.* **7**, 40377 (2017).
28. Swedish Schizophrenia Consortium *et al.* High density methylation QTL analysis in human blood via next-generation sequencing of the methylated genomic DNA fraction. *Genome Biol.* **16**, 291 (2015).

medRxiv preprint doi: https://doi.org/10.1101/2024.08.12.24311885; this version posted August 13, 2024. The copyright holder for this preprint (which was not certified by peer review) is the author/funder, who has granted medRxiv a license to display the preprint in perpetuity. All rights reserved. No reuse allowed without permission.

29. Shi, J. *et al.* Characterizing the genetic basis of methylome diversity in histologically normal human lung tissue. *Nat. Commun.* **5**, 3365 (2014).

30. Dai, J. Y. *et al.* DNA methylation and cis-regulation of gene expression by prostate cancer risk SNPs. *PLoS Genet.* **16**, e1008667 (2020).

31. Schulz, H. *et al.* Genome-wide mapping of genetic determinants influencing DNA methylation and gene expression in human hippocampus. *Nat. Commun.* **8**, 1511 (2017).

32. Houseman, E. A. *et al.* DNA methylation arrays as surrogate measures of cell mixture distribution. *BMC Bioinformatics* **13**, 86 (2012).

33. Fortin, J.-P., Triche Jr, T. J. & Hansen, K. D. Preprocessing, normalization and integration of the Illumina HumanMethylationEPIC array with minfi. *Bioinformatics* **33**, 558–560 (2017).

34. Jakubzick, C. V., Randolph, G. J. & Henson, P. M. Monocyte differentiation and antigen-presenting functions. *Nat. Rev. Immunol.* **17**, 349–362 (2017).

35. Gordon, S. & Taylor, P. R. Monocyte and macrophage heterogeneity. *Nat. Rev. Immunol.* **5**, 953–964 (2005).

36. Tao, L. *et al.* Single-cell RNA sequencing reveals that an imbalance in monocyte subsets rather than changes in gene expression patterns is a feature of postmenopausal osteoporosis. *J. Bone Miner. Res.* zjae065 (2024).

37. Zhou, Y., Deng, H.-W. & Shen, H. Circulating monocytes: an appropriate model for bone-related study. *Osteoporos. Int.* **26**, 2561–2572 (2015).

medRxiv preprint doi: https://doi.org/10.1101/2024.08.12.24311885; this version posted August 13, 2024. The copyright holder for this preprint (which was not certified by peer review) is the author/funder, who has granted medRxiv a license to display the preprint in perpetuity. All rights reserved. No reuse allowed without permission.

38. Marventano, I. *et al.* A complex proinflammatory role for peripheral monocytes in Alzheimer's disease. *J. Alzheimers Dis.* **38**, 403–413 (2014).

39. Yan, P. *et al.* Peripheral monocyte–derived cells counter amyloid plaque pathogenesis in a mouse model of Alzheimer's disease. *J. Clin. Invest.* **132**, (2022).

40. Kawanaka, N. *et al.* CD14+,CD16+ blood monocytes and joint inflammation in rheumatoid arthritis. *Arthritis Rheum.* **46**, 2578–2586 (2002).

41. Pamukcu, B., Lip, G. Y. H., Devitt, A., Griffiths, H. & Shantsila, E. The role of monocytes in atherosclerotic coronary artery disease. *Ann. Med.* **42**, 394–403 (2010).

42. Chittezhath, M. *et al.* Molecular profiling reveals a tumor-promoting phenotype of monocytes and macrophages in human cancer progression. *Immunity* **41**, 815–829 (2014).

43. Fraser, H. B., Lam, L. L., Neumann, S. M. & Kobor, M. S. Population-specificity of human DNA methylation. *Genome Biol.* **13**, R8 (2012).

44. Kato, N. *et al.* Trans-ancestry genome-wide association study identifies 12 genetic loci influencing blood pressure and implicates a role for DNA methylation. *Nat. Genet.* **47**, 1282–1293 (2015).

45. Mozhui, K., Smith, A. K. & Tylavsky, F. A. Ancestry dependent DNA methylation and influence of maternal nutrition. *PloS One* **10**, e0118466 (2015).

46. Greenbaum, J. *et al.* A multiethnic whole genome sequencing study to identify novel loci for bone mineral density. *Hum. Mol. Genet.* **31**, 1067–1081 (2022).

47. Wu, L. *et al.* An integrative multi-omics analysis to identify candidate DNA methylation biomarkers related to prostate cancer risk. *Nat. Commun.* **11**, 3905 (2020).

medRxiv preprint doi: https://doi.org/10.1101/2024.08.12.24311885; this version posted August 13, 2024. The copyright holder for this preprint (which was not certified by peer review) is the author/funder, who has granted medRxiv a license to display the preprint in perpetuity. All rights reserved. No reuse allowed without permission.

48. Baselmans, B. M. *et al.* Multivariate genome-wide analyses of the well-being spectrum. *Nat. Genet.* **51**, 445–451 (2019).

49. Gaziano, J. M. *et al.* Million Veteran Program: A mega-biobank to study genetic influences on health and disease. *J. Clin. Epidemiol.* **70**, 214–223 (2016).

50. Pain, O., Dudbridge, F. & Ronald, A. Are your covariates under control? How normalization can re-introduce covariate effects. *bioRxiv* 137232 (2017).

51. Dahl, A., Guillemot, V., Mefford, J., Aschard, H. & Zaitlen, N. Adjusting for principal components of molecular phenotypes induces replicating false positives. *Genetics* **211**, 1179–1189 (2019).

52. Shabalin, A. A. Matrix eQTL: ultra fast eQTL analysis via large matrix operations. *Bioinformatics* **28**, 1353–1358 (2012).

53. Bomba, L., Walter, K. & Soranzo, N. The impact of rare and low-frequency genetic variants in common disease. *Genome Biol.* **18**, 77 (2017).

54. Zhang, J. *et al.* Plasma proteome analyses in individuals of European and African ancestry identify cis-pQTLs and models for proteome-wide association studies. *Nat. Genet.* **54**, 593–602 (2022).

55. Cavalcante, R. G. & Sartor, M. A. Annotatr: genomic regions in context. *Bioinformatics* **33**, 2381–2383 (2017).

56. Consortium, 1000 Genomes Project. *A Global Reference for Human Genetic Variation*. *Nature* vol. 526 68 (Nature Publishing Group, 2015).

medRxiv preprint doi: https://doi.org/10.1101/2024.08.12.24311885; this version posted August 13, 2024. The copyright holder for this preprint (which was not certified by peer review) is the author/funder, who has granted medRxiv a license to display the preprint in perpetuity. All rights reserved. No reuse allowed without permission.

57. Wang, G., Sarkar, A., Carbonetto, P. & Stephens, M. A Simple New Approach to Variable Selection in Regression, with Application to Genetic Fine Mapping. *J. R. Stat. Soc. Ser. B Stat. Methodol.* **82**, 1273–1300 (2020).

58. Yang, J., Lee, S. H., Goddard, M. E. & Visscher, P. M. GCTA: a tool for genome-wide complex trait analysis. *Am. J. Hum. Genet.* **88**, 76–82 (2011).

59. Noguera-Castells, A., García-Prieto, C. A., Álvarez-Errico, D. & Esteller, M. Validation of the new EPIC DNA methylation microarray (900K EPIC v2) for high-throughput profiling of the human DNA methylome. *Epigenetics* **18**, 2185742 (2023).

60. Bibikova, M. *et al.* High density DNA methylation array with single CpG site resolution. *New Genomic Technol. Appl.* **98**, 288–295 (2011).

61. Chen, B. H. & Zhou, W. mLiftOver: Harmonizing Data Across Infinium DNA Methylation Platforms. *bioRxiv* 2024–03 (2024).

62. Satomi, K., Ichimura, K. & Shibahara, J. Decoding the DNA methylome of central nervous system tumors: An emerging modality for integrated diagnosis. *Pathol. Int.* **74**, 51–67 (2024).

63. Vavourakis, C. D., Herzog, C. M. & Widschwendter, M. Devising reliable and accurate epigenetic clocks: choosing the optimal computational solution. (2023).

64. Zou, H. & Hastie, T. Regularization and variable selection via the elastic net. *J. R. Stat. Soc. Ser. B Stat. Methodol.* **67**, 301–320 (2005).

65. Gamazon, E. R. *et al.* A gene-based association method for mapping traits using reference transcriptome data. *Nat. Genet.* **47**, 1091–1098 (2015).

medRxiv preprint doi: https://doi.org/10.1101/2024.08.12.24311885; this version posted August 13, 2024. The copyright holder for this preprint (which was not certified by peer review) is the author/funder, who has granted medRxiv a license to display the preprint in perpetuity. All rights reserved. No reuse allowed without permission.

66. Mai, J., Lu, M., Gao, Q., Zeng, J. & Xiao, J. Transcriptome-wide association studies: recent advances in methods, applications and available databases. *Commun. Biol.* **6**, 899 (2023).

67. Yao, S. *et al.* A transcriptome-wide association study identifies susceptibility genes for Parkinson's disease. *Npj Park. Dis.* **7**, 79 (2021).

68. Wu, L. *et al.* A transcriptome-wide association study of 229,000 women identifies new candidate susceptibility genes for breast cancer. *Nat. Genet.* **50**, 968–978 (2018).

69. Liu, Y. *et al.* ACAT: a fast and powerful p value combination method for rare-variant analysis in sequencing studies. *Am. J. Hum. Genet.* **104**, 410–421 (2019).

70. Wu, C., Bradley, J., Li, Y., Wu, L. & Deng, H.-W. A gene-level methylome-wide association analysis identifies novel Alzheimer's disease genes. *Bioinformatics* **37**, 1933–1940 (2021).

71. del Bosque-Plata, L., Martínez-Martínez, E., Espinoza-Camacho, M. Á. & Gragnoli, C. The role of TCF7L2 in type 2 diabetes. *Diabetes* **70**, 1220–1228 (2021).

72. Savic, D. *et al.* Alterations in TCF7L2 expression define its role as a key regulator of glucose metabolism. *Genome Res.* **21**, 1417–1425 (2011).

73. Yan, R. *et al.* A novel type 2 diabetes risk allele increases the promoter activity of the muscle-specific small ankyrin 1 gene. *Sci. Rep.* **6**, 25105 (2016).

74. Harder, M. N. *et al.* Type 2 diabetes risk alleles near BCAR1 and in ANK1 associate with decreased β-cell function whereas risk alleles near ANKRD55 and GRB14 associate with decreased insulin sensitivity in the Danish Inter99 cohort. *J. Clin. Endocrinol. Metab.* **98**, E801–E806 (2013).

medRxiv preprint doi: https://doi.org/10.1101/2024.08.12.24311885; this version posted August 13, 2024. The copyright holder for this preprint (which was not certified by peer review) is the author/funder, who has granted medRxiv a license to display the preprint in perpetuity. All rights reserved. No reuse allowed without permission.

75. Freathy, R. M. *et al.* Common variation in the FTO gene alters diabetes-related metabolic traits to the extent expected given its effect on BMI. *Diabetes* **57**, 1419–1426 (2008).

76. Guo, S. *et al.* Inactivation of specific β cell transcription factors in type 2 diabetes. *J. Clin. Invest.* **123**, 3305–3316 (2013).

77. Saxena, R. *et al.* Large-scale gene-centric meta-analysis across 39 studies identifies type 2 diabetes loci. *Am. J. Hum. Genet.* **90**, 410–425 (2012).

78. Hanson, R. L. *et al.* 1642-P: Colocalization Analyses of Genetic Associations of Type 2 Diabetes with DNA Methylation on Chromosome 11p in American Indians. *Diabetes* **69**, (2020).

79. Caballero, B., Finer, N. & Wurtman, R. J. Plasma amino acids and insulin levels in obesity: response to carbohydrate intake and tryptophan supplements. *Metabolism* **37**, 672–676 (1988).

80. Wijekoon, E. P., Skinner, C., Brosnan, M. E. & Brosnan, J. T. Amino acid metabolism in the Zucker diabetic fatty rat: effects of insulin resistance and of type 2 diabetes. *Can. J. Physiol. Pharmacol.* **82**, 506–514 (2004).

81. She, P. *et al.* Obesity-related elevations in plasma leucine are associated with alterations in enzymes involved in branched-chain amino acid metabolism. *Am. J. Physiol.-Endocrinol. Metab.* **293**, E1552–E1563 (2007).

82. Libby, P. & Theroux, P. Pathophysiology of Coronary Artery Disease. *Circulation* **111**, 3481–3488 (2005).

medRxiv preprint doi: https://doi.org/10.1101/2024.08.12.24311885; this version posted August 13, 2024. The copyright holder for this preprint (which was not certified by peer review) is the author/funder, who has granted medRxiv a license to display the preprint in perpetuity. All rights reserved. No reuse allowed without permission.

83. Ghattas, A., Griffiths, H. R., Devitt, A., Lip, G. Y. H. & Shantsila, E. Monocytes in Coronary Artery Disease and Atherosclerosis. *J. Am. Coll. Cardiol.* **62**, 1541–1551 (2013).

84. Schlitt, A. *et al.* CD14+CD16+ monocytes in coronary artery disease and their relationship to serum TNF-α levels. *Thromb. Haemost.* **92**, 419–424 (2004).

85. Gil, J. & Peters, G. Regulation of the INK4b–ARF–INK4a tumour suppressor locus: all for one or one for all. *Nat. Rev. Mol. Cell Biol.* **7**, 667–677 (2006).

86. Huang, K. *et al.* Effects of *CDKN2B-AS1* polymorphisms on the susceptibility to coronary heart disease. *Mol. Genet. Genomic Med.* **7**, e955 (2019).

87. Yin, Y. *et al.* SDF-1α involved in mobilization and recruitment of endothelial progenitor cells after arterial injury in mice. *Cardiovasc. Pathol.* **19**, 218–227 (2010).

88. Döring, Y., Pawig, L., Weber, C. & Noels, H. The CXCL12/CXCR4 chemokine ligand/receptor axis in cardiovascular disease. *Front. Physiol.* **5**, 88349 (2014).

89. Runmin, G. *et al.* Genetic variation of CXCR4 and risk of coronary artery disease: epidemiological study and functional validation of CRISPR/Cas9 system. *Oncotarget* **9**, 14077 (2018).

90. Collaboration, I. G. C. E. R. F. Interleukin-6 receptor pathways in coronary heart disease: a collaborative meta-analysis of 82 studies. *The Lancet* **379**, 1205–1213 (2012).

91. Chen, C. *et al.* Serum TGF-β1 and SMAD3 levels are closely associated with coronary artery disease. *BMC Cardiovasc. Disord.* **14**, 18 (2014).

medRxiv preprint doi: https://doi.org/10.1101/2024.08.12.24311885; this version posted August 13, 2024. The copyright holder for this preprint (which was not certified by peer review) is the author/funder, who has granted medRxiv a license to display the preprint in perpetuity. All rights reserved. No reuse allowed without permission.

92. Zhao, H. *et al.* Proteome-wide Mendelian randomization in global biobank meta-analysis reveals multi-ancestry drug targets for common diseases. *Cell Genomics* **2**, (2022).

93. Giambartolomei, C. *et al.* Bayesian test for colocalisation between pairs of genetic association studies using summary statistics. *PLoS Genet.* **10**, e1004383 (2014).

94. Loyfer, N. *et al.* A DNA methylation atlas of normal human cell types. *Nature* **613**, 355–364 (2023).

95. Tsai, P.-C. & Bell, J. T. Power and sample size estimation for epigenome-wide association scans to detect differential DNA methylation. *Int. J. Epidemiol.* **44**, 1429–1441 (2015).

96. Singmann, P. *et al.* Characterization of whole-genome autosomal differences of DNA methylation between men and women. *Epigenetics Chromatin* **8**, 43 (2015).

97. Grant, O. A., Wang, Y., Kumari, M., Zabet, N. R. & Schalkwyk, L. Characterising sex differences of autosomal DNA methylation in whole blood using the Illumina EPIC array. *Clin. Epigenetics* **14**, 62 (2022).

98. Li, H. & Durbin, R. Fast and accurate short read alignment with Burrows–Wheeler transform. *bioinformatics* **25**, 1754–1760 (2009).

99. DePristo, M. A. *et al.* A framework for variation discovery and genotyping using next-generation DNA sequencing data. *Nat. Genet.* **43**, 491–498 (2011).

100. McKenna, A. *et al.* The Genome Analysis Toolkit: a MapReduce framework for analyzing next-generation DNA sequencing data. *Genome Res.* **20**, 1297–1303 (2010).

medRxiv preprint doi: https://doi.org/10.1101/2024.08.12.24311885; this version posted August 13, 2024. The copyright holder for this preprint (which was not certified by peer review) is the author/funder, who has granted medRxiv a license to display the preprint in perpetuity. All rights reserved. No reuse allowed without permission.

101. Gordon, S. & Taylor, P. R. Monocyte and macrophage heterogeneity. *Nat. Rev. Immunol.* **5**, 953–964 (2005).

102. Yin, Y. *et al.* Impact of cytosine methylation on DNA binding specificities of human transcription factors. *Science* **356**, eaaj2239 (2017).

103. Xi, Y. & Li, W. B. whole genome bisulfite sequence MAPping program. BMC 1027. *Bioinformatics* **10**, 1028 (2009).

104. Martin, M. Cutadapt removes adapter sequences from high-throughput sequencing reads. *EMBnet J.* **17**, 10–12 (2011).

105. Langmead, B. & Salzberg, S. L. Fast gapped-read alignment with Bowtie 2. *Nat. Methods* **9**, 357–359 (2012).

106. Kim, D., Langmead, B. & Salzberg, S. L. HISAT: a fast spliced aligner with low memory requirements. *Nat. Methods* **12**, 357–360 (2015).

107. Pertea, M. *et al.* StringTie enables improved reconstruction of a transcriptome from RNA-seq reads. *Nat. Biotechnol.* **33**, 290–295 (2015).

108. Racle, J., de Jonge, K., Baumgaertner, P., Speiser, D. E. & Gfeller, D. Simultaneous enumeration of cancer and immune cell types from bulk tumor gene expression data. *elife* **6**, e26476 (2017).

109. Min, J. L. *et al.* Genomic and phenotypic insights from an atlas of genetic effects on DNA methylation. *Nat. Genet.* **53**, 1311–1321 (2021).

110. Aberg, K. A. *et al.* Convergence of evidence from a methylome-wide CpG-SNP association study and GWAS of major depressive disorder. *Transl. Psychiatry* **8**, 162 (2018).

medRxiv preprint doi: https://doi.org/10.1101/2024.08.12.24311885; this version posted August 13, 2024. The copyright holder for this preprint (which was not certified by peer review) is the author/funder, who has granted medRxiv a license to display the preprint in perpetuity. All rights reserved. No reuse allowed without permission.

111. Krstajic, D., Buturovic, L. J., Leahy, D. E. & Thomas, S. Cross-validation pitfalls when selecting and assessing regression and classification models. *J. Cheminformatics* **6**, 10 (2014).

112. Xue, H., Shen, X. & Pan, W. Causal Inference in Transcriptome-Wide Association Studies with Invalid Instruments and GWAS Summary Data. *J. Am. Stat. Assoc.* **118**, 1525–1537 (2023).

113. Wu, C., Zhang, Z., Yang, X. & Zhao, B. Large-scale imputation models for multi-ancestry proteome-wide association analysis. *bioRxiv* 2023–10 (2023).

114. Zhao, H. *et al.* Proteome-wide Mendelian randomization in global biobank meta-analysis reveals multi-ancestry drug targets for common diseases. *Cell Genomics* **2**, (2022).

115. Hemani, G., Tilling, K. & Davey Smith, G. Orienting the causal relationship between imprecisely measured traits using GWAS summary data. *PLoS Genet.* **13**, e1007081 (2017).

116. Lawlor, D. A., Harbord, R. M., Sterne, J. A. C., Timpson, N. & Davey Smith, G. Mendelian randomization: Using genes as instruments for making causal inferences in epidemiology. *Stat. Med.* **27**, 1133–1163 (2008).